The Astrophysical Journal, 570:329–343, 2002 May 1
© 2002. The American Astronomical Society. All rights reserved. Printed in U.S.A.

STRUCTURE, EVOLUTION, AND NUCLEOSYNTHESIS OF PRIMORDIAL STARS

Lionel Siess,[1, 2, 3, 4] Mario Livio,[2] and John Lattanzio[3]

Received 2001 July 16; accepted 2002 January 14

ABSTRACT

The evolution of Population III stars ($Z = 0$) is followed from the pre–main-sequence phase up to the asymptotic giant branch (AGB) phase for intermediate-mass stars and up to C ignition in more massive stars. Our grid includes 11 stars, covering the mass range 0.8–20 $M_{\odot}$. During the H and He core burning phases an overshooting characterized by $d = 0.20H_P$ was applied, and during the AGB phase a small extension of the convective envelope was also allowed, characterized by $d = 0.05H_P$. We find that at the beginning of the AGB phase, following the development of a convective instability in the He-burning shell, a secondary convective zone forms at the He-H discontinuity. This unusual convective zone then expands and overlaps with the region previously occupied by the receding He-driven instability. Carbon is engulfed and an H flash takes place as a result of the activation of the CNO cycle. Following these successive (H + He) flashes, the convective envelope penetrates deeper into the star, reaches the secondary H convective shell, and allows CNO catalysts to be dredged up to the surface. These mixing episodes, which have been found to occur in our 1, 1.5, 2, 3, 4, and 5 $M_{\odot}$ models, increase the carbon abundance in the envelope and allow low- and intermediate-mass stars to achieve a "standard" thermally pulsing AGB phase, confirming the recent results by Chieffi and collaborators. We also find that at the beginning of the double shell burning evolution, our 4 and 5 $M_{\odot}$ models experience so-called degenerate thermal pulses, which are very similar to those found by Frost et al. but absent from the Chieffi et al. simulations. Finally, in the 7 $M_{\odot}$ model, the CNO envelope abundance following the second dredge-up is so large that the star does not experience the carbon injection episode and follows a standard thermally pulsing AGB evolution. Our computations also indicate that, thanks to the small overshooting at the base of the convective envelope, the third dredge-up is already operating in stars with $M \geq 1.5\ M_{\odot}$ after a few pulses, and that by the end of our modeling, hot bottom burning is activated in stars more massive than $\sim 2\ M_{\odot}$. This evolutionary behavior suggests that primordial low- and intermediate-mass stars could have been significant contributors to the production of primary ^{12}C and ^{14}N and may have contributed to some extent to the production of Mg and Al and possibly *s*-process elements (despite the lack of iron seeds) in the early universe.

Subject headings: cosmology: theory — nuclear reactions, nucleosynthesis, abundances — stars: abundances — stars: evolution — stars: interiors

On-line material: color figures

1. INTRODUCTION

The first stars that formed in our universe, commonly referred to as Population III stars, have a composition given by the products of the big bang nucleosynthesis and are essentially made of hydrogen and helium with some traces of lithium. A major issue concerning primordial stars is the determination of the initial mass function (IMF). In the absence of heavy elements and dust grains, the cooling mechanisms may indeed be less efficient and favor the formation of massive or very massive stars (e.g., Silk 1977; Bromm, Coppi, & Larson 1999). However, it has also been shown (e.g., Carlberg 1981; Palla, Salpeter, & Stahler 1983) that even a small fraction of molecular hydrogen can provide a significant contribution to the cooling due to rotational and vibrational transitions. The resulting Jeans mass of a pure H and He cloud can then be relatively small and may even fall below 0.1 $M_{\odot}$. Yoshii & Saio (1986), using the opacity-limited fragmentation theory of Silk (1977), estimate the peak mass of the IMF to be around 4–10 $M_{\odot}$. Based on one-dimensional hydrodynamical simulations of a collapsing cloud, Nakamura & Umemura (1999) find that the typical mass of the first stars is about 3 $M_{\odot}$, which may grow to 16 $M_{\odot}$ by accretion. Extending their previous work by performing two-dimensional simulations, Nakamura & Umemura (2001) reevaluated the IMF and came up with the result that it is likely to be bimodal, with peaks around 1 and 100 $M_{\odot}$. Adopting a different approach based on the effects of a primordial generation of stars on the pollution of the intergalactic medium, Abia et al. (2001) showed that an IMF peaked around 4–8 $M_{\odot}$ is needed to account for the large [C/Fe] and [N/Fe] ratios observed in extremely metal-poor stars. Therefore, the mass scale of Population III stars still remains relatively uncertain, and it is possible that even very low mass stars ($M \lesssim 0.8\ M_{\odot}$) might have survived up to present day as nuclear burning stars.

In the early universe, low- and intermediate-mass stars actively contributed to the enrichment of the interstellar medium, and an understanding of their evolution and nucleosynthesis is absolutely essential for a comprehension of the chemical evolution of the universe. On the theoretical side,

[1] Institut d'Astronomie et d'Astrophysique CCP 226, Université Libre de Bruxelles, B-1050 Brussels, Belgium.

[2] Space Telescope Science Institute, 3700 San Martin Drive, Baltimore, MD 21218.

[3] Department of Mathematics and Statistics, Monash University, Clayton, Victoria 3168, Australia.

[4] Groupe de Recherche en Astronomie et Astrophysique, Université de Montpellier II, CC072, F-34095 Montpellier Cedex 5, France; siess@astro.ulb.ac.be.

several works have been devoted to the study of the structure and evolution of primordial stars, and we refer the reader to the recent reviews by Castellani (2000) and Chiosi (2000) for a description of these previous investigations.

In this paper we present and analyze computations of zero-metallicity stars, using a state-of-the-art code, thus continuing and completing the previous studies. In § 2 we describe briefly the physics of the stellar evolution code, and in § 3 we analyze the structure and evolution of the primordial stars. We also make a careful comparison of our results with those from previous computations. In § 4 we describe the evolution of the surface chemical composition in relation to the chemical history of the universe and then conclude.

2. NUMERICAL COMPUTATIONS

The Grenoble stellar evolution code has been used for these computations. For a detailed discussion of its input physics, we refer the reader to several papers published by the group (Forestini & Charbonnel 1997; Siess, Dufour, & Forestini 2000). Briefly, in the domain of high temperatures (>8000 K) we use the OPAL opacity tables (Iglesias & Rogers 1996), which are adequate for enhanced values of C and O. Thus, when the C and O abundances are modified, e.g., during the third dredge-up (3DUP) events, their effects on the opacity are taken into account.

The conductive opacities are computed from a modified version of the Iben (1975) fits to the Hubbard & Lampe (1969) tables for nonrelativistic electrons, from Itoh et al. (1983) and Mitake, Ichimaru, & Itoh (1984) for relativistic electrons, and from formulae of Itoh et al. (1984) as well as Raikh & Yakovlev (1982) for solid plasmas. Below 8000 K, we use the atomic and molecular opacities provided by Alexander & Fergusson (1994). The equation of state (EOS) follows the formalism developed by Pols et al. (1995) and provides an accurate treatment of the nonideal effects, especially the treatment of pressure ionization and degeneracy in partially ionized plasma (see, e.g., Siess et al. 2000 for a detailed discussion and for the tests of this EOS).

The nuclear network includes 180 nuclear (neutron, proton, and ^{4}He captures) and decay reactions, and we follow the abundance evolution of 52 nuclides. Most of the reaction rates that originally came from Caughlan & Fowler (1988) have recently been updated using the NACRE compilation (Angulo et al. 1999). Finally, the nuclear screening factors are parameterized using the Graboske et al. (1973) formalism, including weak, intermediate, and strong screening cases, and the computations are stopped in the massive stars ($M \gtrsim 10\ M_\odot$) at C ignition when the temperature reaches 8×10^8 K.

The surface boundary conditions are treated in the gray atmosphere approximation, and we use the de Jager mass-loss rate prescription (de Jager, Nieuwenhuijzen, & van der Hucht 1988). However, because of the lack of metals, the mass-loss rate only activates during the late stages of the asymptotic giant branch (AGB) phase.

We use the standard mixing length theory (Cox & Guili 1968) with $\alpha_{\rm MLT} = 1.5$, and we follow the Schaller et al. (1992) suggestion and account for a moderate overshooting characterized by $d = 0.20 H_P$ during the central H- and He-burning phases. During the AGB phase, the extent of the convective envelope has also been increased by assuming a moderate overshooting characterized by $d = 0.05 H_P$. This choice was made as a way of obtaining a stable Schwarzschild boundary for the envelope in a simple and consistent way and is similar to the work of Herwig, Blocker, & Driebe (1999).

The chemical composition of our initial models is characterized by $X = 0.765$, $Y = 0.235$ and by a ^{7}Li mass fraction $X_{\rm Li} = 9.26 \times 10^{-10}$. These values (Burles & Tytler 1998; Bonifacio & Molaro 1997) are taken from big bang nucleosynthesis calculations. Finally, inside convective zones, the chemical species are homogeneously mixed.

For numerical details, the code uses an adaptive mesh point. Different criteria regulate the zoning, and, in particular, shells are added in regions where the gradients of energy production and chemical composition are steep. Typically, the region of mixing episodes is described by ≈500 shells, and depending on the evolutionary status, the structure is discretized into 1000–3500 shells. The time step is constrained so that the relative variations of the independent variables, between one model and the next, do not exceed 10% and the luminosity does not differ by more than 5%. During the convergence process, the equations of stellar structure must be satisfied at least to a 10^{-3} level of precision.

3. STRUCTURAL EVOLUTION OF LOW- AND INTERMEDIATE-MASS STARS

In this section we describe the structure and evolution of low- and intermediate-mass stars through the computations of 1 and 5 $M_\odot$ models. These models were chosen so as to enable comparison with other works. First we analyze the evolution during the core H and He burning, then we describe the AGB phase, and finally we summarize the nucleosynthesis occurring in these stars.

3.1. *Evolution of Low-Mass Stars:* 1 $M_\odot$ *Model*

During the pre–main-sequence contraction phase, the small amount of primordial ^{7}Li is burnt by proton captures to helium. After 12.5 Myr,[5] the central temperature reaches $\simeq 10^7$ K and a convective core of $\simeq 0.20\ M_\odot$ forms. There H is burnt mainly by the PPI (97%) chain, which is later supplemented by the PPIII chain. After 3.72×10^9 yr the convective core disappears, and owing to the increased temperature, carbon production by the 3α reaction starts. When the central carbon mass fraction reaches 1.8×10^{-12} ($T_c = 6.37 \times 10^7$ K), the CN cycle ultimately ignites.

The shifting of the nuclear energy production from the *p-p* chain to the CNO cycle takes place roughly at the same carbon abundance threshold. This is illustrated in Figure 1, which depicts the evolution of the central carbon abundance as a function of central H abundance. The curves show a bump around a similar value of $\log X(^{12}{\rm C}) \simeq -11.5$. This indicates an increase in the H mass fraction, which results from the development of the convective core, corresponding to the ignition of the CNO reactions. We can see that stars with $M \geq 3\ M_\odot$ ignite the CNO cycle relatively early in the evolution, when the central H abundance $X \geq 0.1$. On the other hand, stars less massive than $\sim 1\ M_\odot$ never ignite CNO reactions during their main sequence.

[5] The age "zero" corresponds to the time we started the computations, from a polytropic model located on the Hayashi line.

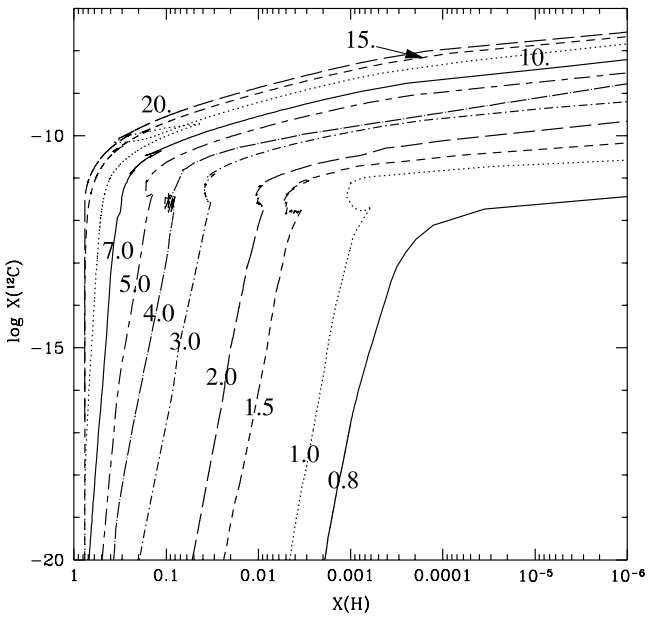

FIG. 1.—Central carbon abundance as a function of central H abundance (in mass fraction). From right to left the different curves correspond to stellar masses equal to 0.8, 1.0, 1.5, 2, 3, 4, 5, 7, 10, 15, and 20 $M_\odot$. The ignition of the CNO cycle during the main sequence occurs when $\log(^{12}\mathrm{C}) \simeq -11.5$ and can be identified by the bump in the different curves, which corresponds to the appearance of a convective core.

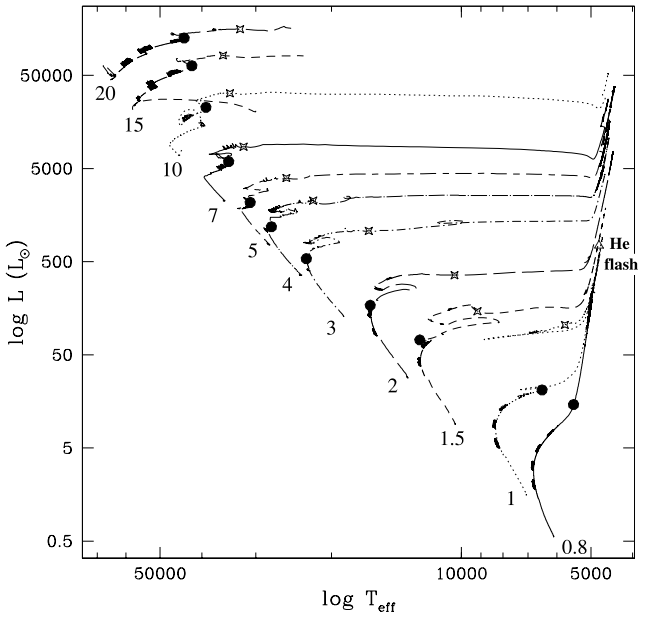

FIG. 2.—H-R diagram for the complete set of $Z = 0$ evolutionary tracks, from 0.8 to 20 $M_\odot$. The filled circles and open stars on the tracks indicate the end of the H and He core burning phases, respectively. The 0.8 and 1.0 $M_\odot$ models experience the first dredge-up and at the tip of their RGB undergo the He flash (triangle in case of the 1 $M_\odot$ model). [*See the electronic edition of the Journal for a color version of this figure*.]

The steep temperature dependence of these reactions leads to the development of a new convective core that lasts for ≈16 Myr in our 1 $M_\odot$ model. During this "CNO flash," the star exhibits a blue loop in the H-R diagram, and, according to Fujimoto, Iben, & Hollowell (1990, hereafter FIH90), it can be explained as follows. At the ignition of the CN cycle, the core expands and both density and temperature decrease in the central regions. The surface layers thus contract and the star moves to the blue side of the H-R diagram. As the flash decays, core contraction resumes, gravitational energy is released, and a new expansion takes place; the star moves back to the red side of the H-R diagram, producing the loop. When the red giant branch (RGB) is reached, the convective envelope deepens and the first dredge-up occurs. Note that only stars with $M \lesssim 1.0\ M_\odot$ experience the first dredge-up. Its effect on the surface composition is marginal and amounts to a slight enrichment in ^{3}He and ^{4}He and to the destruction of the remaining ^{7}Li.

The evolutionary tracks of $Z = 0$ stars in the H-R diagram are presented in Figure 2. The appearance of blue loops in the tracks is present at the end of the main sequence of our 1 $M_\odot$ model and also in the 3, 4, and marginally 5 $M_\odot$ models at the ignition of the CNO cycle in the H-burning shell (HBS) at the beginning of the AGB phase. Note also that because of the lower opacity of the envelope, zero-metallicity stars have a substantially higher effective temperature than their counterparts of higher metallicity. Their UV flux is substantially larger, and massive primordial stars are now considered to be the leading candidates for the sources of reionization of the intergalactic medium (e.g., Gnedin 2000).

The evolution of a $Z = 0$ solar mass star has recently been modeled by Weiss et al. (2000, hereafter W00), who compared their work with the earlier simulation of FIH90. We will not reproduce that comparison here but rather extend it by comparing our model with the most recent simulation of W00. During the central H-burning phase, the main difference is the development of a convective core in our 1 $M_\odot$ model, a feature absent from both the W00 and the FIH90 simulations. The presence of this convective region may simply arise from the adoption of different input physics and leads to slightly lower central temperatures and densities. It also affects the age at the turnoff, which is slightly larger in our models (6.56 Gyr in comparison with 6.31 Gyr found by W00). At the ignition of the CNO cycle, we find a similar hydrogen concentration at the center ($X_c = 5.8 \times 10^{-4}$), and the maximum size of the CNO-driven convective core is also very comparable (∼0.11 $M_\odot$ in W00, in comparison with ∼0.095 $M_\odot$ in this study). The smaller core size characterizing our models is probably a consequence of our lower central temperatures. For comparison, at the maximum nuclear energy production during the flash, the central abundances of $^{12}\mathrm{C} : ^{14}\mathrm{N} : ^{16}\mathrm{O}$ are $8.30 \times 10^{-12} : 2.48 \times 10^{-10} : 2.78 \times 10^{-12}$ in our models and $6.50 \times 10^{-12} : 2.19 \times 10^{-10} : 2.77 \times 10^{-12}$ in W00. Finally, during the "CNO flash" the luminosity generated by the CN cycle (L_{CNO}) remains always smaller than the one generated by the *p*-*p* reactions. At its peak, L_{CNO} represents about 16% of the total nuclear energy production. The contribution due to He burning is negligible ($L_{\mathrm{He}} \simeq 10^{-7}\ L_\odot$) and is slightly less than in W00 ($L_{\mathrm{He}} = 2.6 \times 10^{-7}\ L_\odot$) but still 2 orders of magnitude smaller than in FIH90.

As far as the RGB evolution is concerned, we did not encounter the thermal instabilities in the HBS found by FIH90. Even forcing the time step not to exceed 10^{10} s, we did not find, similarly to W00, the instabilities found by FIH90. Finally, at the time of the He flash, the general properties of our model are very similar to those of W00, the

luminosity and hydrogen-exhausted core mass being 227.75 compared to 229.4 $L_\odot$ and 0.497 compared to 0.492 $M_\odot$, respectively.

The ignition of core He burning starts off-center at a mass coordinate $M_r = 0.31\ M_\odot$, which is slightly larger than the 0.25 and 0.27 $M_\odot$ found by D'Antona (1982) and Cassisi & Castellani (1993), respectively, but significantly smaller than the 0.41 $M_\odot$ found by FIH90. The location where the first He shell flash starts has important consequences for the subsequent evolution. Indeed, if the He flash ignites close enough to the H discontinuity, as has been found by FIH90 and later by Fujimoto, Ikeda, & Iben (2000) and Schlattl et al. (2001), the He-driven convective zone might be able to penetrate the overlying H-rich layers. In this situation, protons are engulfed in the He-driven convective zone, mixed with the abundant carbon, and an H flash occurs that subsequently leads to large modifications in the surface chemical composition and in particular to a large C and N enrichment. The location where the He flash ignites is thus a crucial issue, but it depends on the star's internal structure, which in turn reflects the imprint of the adopted physics. Recently, Schlattl et al. (2001) have analyzed in detail the conditions for proton ingestion during the He core flash. Their analysis reveals that the occurrence of this phenomenon depends quite significantly on the initial conditions. More specifically, they showed that the use of a different EOS (which determines the electron degeneracy), the use of different radiative and/or conductive opacity tables, or the treatment or not of diffusion can trigger or inhibit the penetration of the He-driven flash into the H-rich layers. They also showed that the treatment of convection has very little effect on the outcome. As emphasized in FIH90, the use of different treatments of plasma neutrinos turns out to have significant effects on the results. Finally, we recall that the location of the He flash also depends on the rate at which the HBS advances in mass. Since there are several differences in physical input between FIH90 and the present work (which include core overshooting), it is not easy to give a unique explanation for this different location, but we suspect that the opacities may have played a dominant role. To conclude, we did not find proton mixing because our He ignites too far from the H-He discontinuity; to illustrate the entangled dependence of this phenomenon on the initial conditions, let us note that Marigo et al. (2001) did not mention any evidence of extra protons mixing during the He core flash of their low-mass stars.

The flash is initiated at the point of maximum temperature. Where the degeneracy is lifted, the temperature increases very rapidly and the nuclear energy production due to 3α reactions undergoes a runaway. A convective instability develops and the stellar structure expands. The pressure and the temperature in the degenerate core decrease as the weight of the overlying layers decreases, and when the flash dies away, core contraction resumes. The temperature peak then moves inward and advances in mass by $\sim 0.03\ M_\odot$ between each secondary flash, a value very similar to the one found by Mengel & Sweigart (1981) in their 0.70 $M_\odot$ stellar model.

Figure 3 illustrates the sequence of events that precedes central He burning. A series of 10 convective instabilities progressively lift the degeneracy in the core. The first flash is the strongest as a result of the higher core degeneracy at that time and has the largest extent. The extension in mass of the subsequent flashes is smaller as a result of the lower He

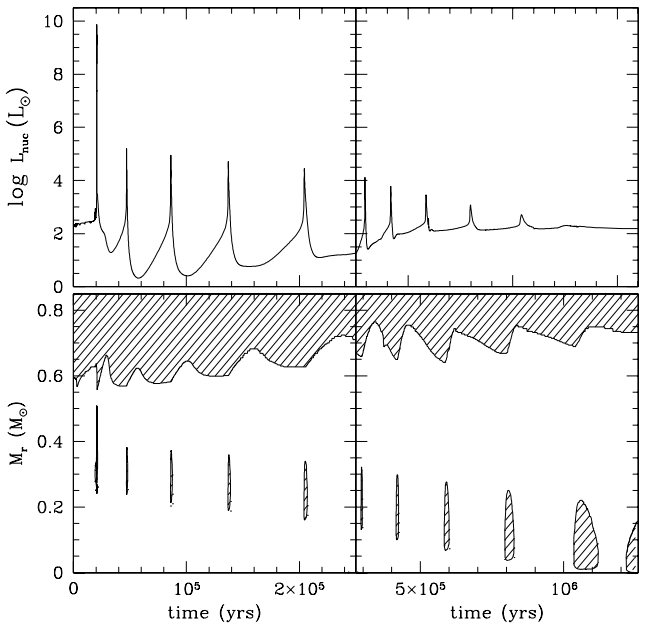

FIG. 3.—Evolution of the convective regions (*lower panels*) and of the nuclear luminosity (*upper panels*) of the 1 $M_\odot$ model during the He core flash. Convective regions are represented by hatched areas.

luminosity, and the time interval between the secondary flashes also gradually increases (see also Despain 1981). Table 1 summarizes the characteristics of these flashes.

During the major flash, only a very small amount of protons is ingested into the convective region, and this prevents the H-burning luminosity from reaching the very high values encountered in the computations of Hollowell, Iben, & Fujimoto (1990) and Fujimoto et al. (2000). Our computations show that the H mass fraction at the outermost point of the convective region is always smaller than $X < 10^{-8}$ and the hydrogen-generated luminosity never exceeds $\sim 10^4$ $L_\odot$ at its peak. The maximum extent of the convective flash reaches to within 0.005 $M_\odot$ of the H-rich region (where $X > 0.1$), which is located at $M_r = 0.5075\ M_\odot$.

After 10 flashes, He burning starts at the center and the star rapidly moves to the blue side of the H-R diagram along the horizontal branch. The envelope recedes, and a convec-

TABLE 1
CHARACTERISTICS OF THE He FLASHES OCCURRING BEFORE CENTRAL He BURNING

Pulse	$L_{\rm nuc}$ ($L_\odot$)	$M_{\rm ignit}$[a]	Duration (yr)
1.....	7×10^9	0.2991	2300
2.....	1.4×10^5	0.2655	1140
3.....	7.9×10^4	0.2487	1700
4.....	5.3×10^4	0.2289	2600
5.....	2.3×10^4	0.1938	3400
6.....	1.4×10^4	0.1740	4500
7.....	6000	0.1420	7900
8.....	2330	0.1145	16900
9.....	1020	0.0886	31500
10.....	400	0.0672	87000

[a] Mass coordinate of the inner border of the convective zone at the ignition of the instability (in $M_\odot$).

tive core of $\sim 0.20\ M_{\odot}$ forms and is sustained for ≈ 70.6 Myr until He is depleted at the center. The energy production comes largely from the 3α reactions (90%) taking place in the core but also in part from gravitational contraction (10%). The HBS, while still active, does not contribute significantly to the net energy budget. During the central He-burning phase, the convective core is subject to "breathing" pulses and convective tongues develop at the surface of the core, adding additional He into the burning region and temporarily increasing the He-burning luminosity.

We present in Table 2 selected parameters for our computed models during the central H- and He-burning phases, namely, the duration of the H (He) core burning phase, the central temperature and density when the central abundance of H (He) equals 0.5, the abundance of the three most abundant species at the end of each core burning phase, the core mass at the tip of the RGB, and the deepest extent of the convective envelope following the He core burning phase. Interestingly, we see that the central density during the H core burning and the core mass at the tip of the RGB show a minimum around $M \simeq 1.5\ M_{\odot}$. This value is very similar to the one found by Cassisi & Castellani (1993) and corresponds to the critical mass for the ignition of He in strongly degenerate conditions. This smaller value for the mass limit, compared, for example, with the $1.8\ M_{\odot}$ found for $Z = 10^{-6}$ (Cassisi & Castellani 1993), results from the fact that more metal-deficient stars must increase their temperature (and density) to sustain a larger luminosity. They are consequently hotter and are thus less affected by electron degeneracy.

The comparison of the nuclear lifetime with the recent paper by Marigo et al. (2001) reveals discrepancies as large as 15% in the duration of the main sequence. The largest shift is found for the critical mass $M = 1.5\ M_{\odot}$, and for this reason we suspect that part of these differences result from the adopted equation of state. Further, these authors use a different value for the overshooting parameter, which can also explain the discrepancies. Globally, our lower mass models ($M \leq 3\ M_{\odot}$) evolve more slowly while the more massive ones tend to evolve slightly faster.

At the end of the central He-burning phase ($t \sim 7.27 \times 10^9$ yr), a CO core of $\sim 0.202\ M_{\odot}$ has formed

TABLE 2

Evolutionary Characteristics of $Z = 0$ Stars

H-burning Phase

		$X = 0.5$ at the Center		$X < 10^{-8}$ at the Center			
Mass	t_H[a] (Myr)	T_c (10^6 K)	$\log \rho_c$	^{12}C	^{14}N	^{16}O	M_{tip}[b] ($M_{\odot}$)
0.8.....	1.48E10	13.9	2.161	2.03 (−10)	3.50 (−10)	1.68 (−11)	0.468[c]
1.0.....	6.85E9	16.7	2.169	7.71 (−10)	1.71 (−9)	1.59 (−10)	0.494
1.5.....	1.89E9	23.2	2.050	8.73 (−10)	3.07 (−9)	2.87 (−10)	0.277
2.0.....	7.42E8	27.8	2.173	8.68 (−10)	7.18 (−9)	5.67 (−10)	0.334
3.0.....	2.12E8	38.9	2.267	7.12 (−9)	2.27 (−8)	2.35 (−9)	0.445
4.0.....	1.04E8	49.1	2.303	9.17 (−8)	1.81 (−8)	1.50 (−8)	0.516
5.0.....	6.14E7	58.8	2.338	1.74 (−6)	1.64 (−7)	2.15 (−8)	0.570
7.0.....	3.16E7	75.0	2.385	8.47 (−6)	3.05 (−7)	4.78 (−8)	0.900
10.....	1.82E7	91.7	2.398	1.16 (−5)	3.88 (−7)	5.79 (−8)	1.491
15.....	1.21E7	100.0	2.152	3.37 (−5)	4.86 (−7)	9.39 (−8)	3.177
20.....	8.77E6	103.7	2.022	1.85 (−4)	6.27 (−7)	2.66 (−7)	5.196

He-burning Phase

		$Y = 0.5$ at the Center		$Y < 10^{-8}$ at the Center			
Mass	t_{He}[d] (Myr)	T_c (10^6 K)	$\log \rho_c$	^{12}C	^{14}N	^{16}O	M_{env}[e] ($M_{\odot}$)
1.0.....	175.6	1.305	4.113	0.294	0.698	7.94 (−3)[f]	0.602
1.5.....	104.8	1.291	4.146	0.194	0.801	4.45 (−3)[f]	0.577
2.0.....	68.3	1.340	4.010	0.259	0.741	1.00 (−5)	0.690
3.0.....	17.7	1.430	3.766	0.378	0.622	3.69 (−6)	0.756
4.0.....	12.0	1.504	3.620	0.424	0.576	3.62 (−6)	0.842
5.0.....	8.8	1.539	3.506	0.372	0.627	6.45 (−6)	0.898
7.0.....	4.0	1.640	3.300	0.380	0.620	1.41 (−5)	1.054
10.....	3.0	1.699	3.132	0.355	0.645	8.30 (−5)	2.380
15.....	0.90	1.877	2.921	0.296	0.704	4.78 (−4)	No DUP
20.....	0.63	1.965	2.818	0.280	0.718	1.06 (−3)	No DUP

[a] Main-sequence duration.

[b] Mass of the H-depleted core at the time of He ignition as defined when $L_{He} > 100\ L_{\odot}$.

[c] At the end of our computations (15 Gyr), this star had not yet ignited its core He supply. The value quoted is for the last computed model.

[d] Duration of core He burning phase.

[e] Mass coordinate of the maximum extent of the convective envelope following the He core burning phase.

[f] In this model, the third most abundant element is ^{22}Ne.

and the star enters the early AGB phase. As core contraction proceeds, the luminosity of the He-burning shells (HeBSs) increases and the HBS is switched off. This situation allows the deepening of the convective envelope, which reaches a mass coordinate of 0.599 $M_{\odot}$. The second dredge-up is a general feature of stars in the mass range $1.0 \leq M < 10\ M_{\odot}$, and its efficiency in polluting the envelope increases with mass. Following this deep mixing, the surface layers are mainly enriched in ^{4}He and to a lesser extent with CNO elements. Table 3 summarizes some of the properties of the envelope composition at the end of this phase.

3.2. *Evolution of Intermediate-Mass Stars: 5 $M_{\odot}$ Model*

The lack of ^{12}C prevents the CN cycle from operating, and during the major phase of central H burning, the dominant source of energy of the star is provided by the *p-p* chains. Because of the relatively weak temperature sensitivity and low efficiency of these reactions, the active burning region ($\varepsilon_{\rm nuc} > 5$ ergs g^{-1} s^{-1}) encompasses a large fraction of the star, up to $\simeq$80% of its mass. At the beginning of the main sequence, a convective core develops and disappears at an age of 41.6 Myr when the central H abundance has been reduced to $X_c \simeq 0.34$. This value is slightly smaller than the one reported by Chieffi & Tornambé (1984), who found $X_c \simeq 0.45$, and the difference can be attributed to the use of different nuclear reaction rates in the earlier work. Indeed, the nuclear reaction rates for the *p-p* reactions provided by the NACRE compilation (Angulo et al. 1999) are either identical to or smaller than the ones used by Chieffi & Tornambé (1984). As a consequence of these slower rates, the temperature must be higher in order to increase the nuclear energy production and balance the stellar energy budget. This explains why our 5 $M_{\odot}$ model is globally hotter and evolves more rapidly than in the computations of Chieffi & Tornambé (1984). The differences in the opacity tables also contribute to increase the discrepancies as illustrated by the duration of the main sequence, which is 35% shorter in our simulations (62.6 Myr in our work compared to 100 Myr). On the other hand, comparisons with the more recent computations of Chieffi et al. (2001, hereafter C01) show a good agreement on the main-sequence lifetime (62 Myr in their simulations), and a close examination of their Figure 2 reveals that during the main core burning phases, the evolutions of the central density and temperature are very similar. However, the duration of the first convective core phase and the central H abundance when it disappears are significantly different (they found 20 Myr and $X_c = 0.5$). Since the input physics of both stellar evolution codes are similar (same nuclear reaction rates and opacity tables) and since we do not expect large differences in the EOS at this evolutionary phase, we attribute this discrepancy as probably due to the presence of overshooting in the present work. During the main sequence, ^{12}C slowly builds up in the

TABLE 3
Selected Properties of Our Thermally Pulsing Stars

Mass	$M_{\rm core}$[a] ($M_{\odot}$)	Surface Mass Fraction				
		H	^{4}He	^{12}C	^{14}N	^{16}O
Prior to First Pulse						
1.0.....	0.4176	0.7603	0.2389	2.67 (−32)	3.46 (−28)	3.18 (−26)
1.5.....	0.4979	0.7300	0.2697	7.57 (−22)	4.57 (−22)	1.22 (−21)
2.0.....	0.6476	0.6924	0.3074	2.71 (−20)	8.43 (−21)	2.84 (−21)
3.0.....	0.6890	0.6421	0.3578	9.63 (−17)	1.09 (−14)	3.06 (−16)
4.0.....	0.7733	0.6348	0.3652	8.92 (−14)	8.99 (−12)	2.27 (−13)
5.0.....	0.8833	0.6205	0.3795	6.873 (−9)	7.72 (−10)	1.18 (−10)
7.0.....	1.0268	0.6236	0.3764	2.409 (−5)	1.444 (−9)	9.390 (−8)
End of Carbon Injection						
1.0.....	0.4968	0.7544	0.2447	9.733 (−6)	7.596 (−5)	1.141 (−4)
1.5.....	0.5041	0.7117	0.2879	4.188 (−7)	1.739 (−5)	2.425 (−7)
2.0.....	0.6662	0.6175	0.3081	1.475 (−7)	5.730 (−6)	5.760 (−8)
3.0[b]	0.7381	0.6421	0.3578	2.65 (−11)	6.91 (−10)	5.59 (−12)
3.0.....	0.7413	0.6421	0.3578	5.69 (−11)	2.247 (−9)	2.29 (−11)
3.0.....	0.7464	0.6421	0.3578	4.95 (−10)	1.814 (−8)	1.91 (−10)
3.0.....	0.7487	0.6421	0.3578	2.193 (−7)	9.312 (−8)	1.846 (−6)
4.0.....	0.8316	0.6342	0.3655	5.043 (−6)	1.527 (−6)	1.419 (−4)
5.0.....	0.8971	0.6204	0.3795	1.163 (−5)	2.071 (−7)	1.524 (−5)
Last Computed Model						
1.0.....	0.627	0.7526	0.2466	7.473 (−4)	7.854 (−5)	2.231 (−4)
1.5.....	0.615	0.6882	0.3019	6.905 (−3)	1.922 (−5)	2.356 (−3)
2.0.....	0.739	0.6811	0.3153	3.376 (−3)	6.718 (−6)	8.515 (−5)
3.0.....	0.812	0.6312	0.3646	4.447 (−4)	3.256 (−3)	1.121 (−4)
4.0.....	0.849	0.6312	0.3660	4.453 (−6)	1.321 (−3)	1.167 (−3)
5.0.....	0.908	0.6187	0.3809	6.138 (−5)	2.963 (−4)	2.317 (−5)
7.0.....	1.059	0.6226	0.3773	8.939 (−6)	7.838 (−5)	1.750 (−6)

[a] Mass at the base of the HeBS.
[b] This model experiences four carbon injections before reaching the TP-AGB phase.

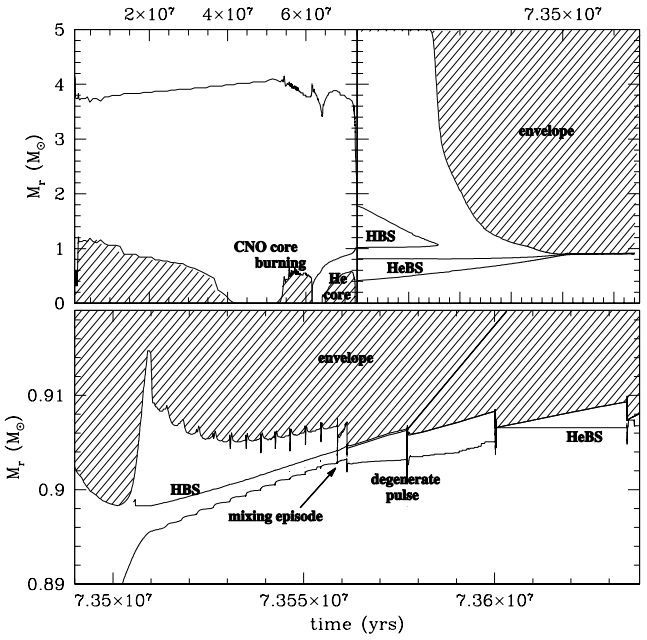

FIG. 4.—Evolution of the structure of the 5 $M_\odot$ model. The hatched areas correspond to a convective region, and the thick solid lines delineate the H- and He-burning regions where $\varepsilon_{\rm nuc} > 5$ ergs g s^{-1}. [*See the electronic edition of the Journal for a color version of this figure.*]

core, and when its central abundance reaches $\simeq 5 \times 10^{-12}$, the CNO cycle comes into play and rapidly takes over the nuclear energy production. Because of the reaction's strong temperature dependence, a central convective zone forms again and extends up to $\sim$0.56 $M_\odot$ (Fig. 4), a value substantially larger than the one found by C01 (0.4 $M_\odot$). Note that during this "convective" period, 3α reactions keep running. They participate only marginally in the nuclear energy production but maintain and increase the central ^{12}C abundance. When the central H mass fraction falls below 5×10^{-6}, the convective core disappears and an HBS forms. Contraction resumes, and after 2.4 Myr a helium convective core develops while the star is still located in the blue side of the H-R diagram. This failure to become a red giant just after central hydrogen depletion prevents the first dredge-up from occurring. During the He-burning phase, the central temperature increases, and when it reaches $T_c \simeq 1.7 \times 10^8$ K, carbon starts to be burnt into ^{16}O by α-captures. At the end of the central He-burning phase, a degenerate core of $\sim$0.6 $M_\odot$ has formed, composed of 37% of ^{12}C and 63% of ^{16}O. Note that the 10 Myr duration of the He-burning phase is very comparable to the 9.8 Myr found by C01.

When He is depleted at the center, the star undergoes a large expansion and moves rapidly to the red side of the H-R diagram. The HBS quenches and the convective envelope deepens. At its largest extent, the envelope reaches a mass coordinate of $M_r \simeq 0.896$ $M_\odot$ and dredges up to the surface the products of the nucleosynthesis taking place in the H burning. As a result of the CNO cycle, the surface is mainly enriched in ^{14}N and ^{4}He, and because the 3α reactions are also at work in the HBS, the abundances of ^{12}C and ^{16}O are increased while H and ^{3}He are depleted. After the reignition of the HBS, the star undergoes a series of "weak" thermal runaways in the HeBS ($L_{\rm He} \lesssim 10^5$ $L_\odot$) that are not powerful enough to trigger the formation of a convective region or to extinguish the HBS (Fig. 4). However, at the 13th instability, a convective region forms in the HeBS, and by the mechanism described in the next section, a pollution of the envelope takes place, allowing the star to resume a "standard" AGB evolution. Interestingly, Chieffi & Tornambé (1984) also found that four small instabilities developed in their 5 $M_\odot$ model at the beginning of the AGB phase. However, these authors did not find subsequent mixing, and a steady state double shell burning evolution followed, characterized by the absence of thermal pulses.

After the H reignition, the luminosity is mostly provided by the HBS (75%) and to a lesser extent by the HeBS (15%) and gravitational contraction (10%). When the temperature in the HBS reaches 10^8 K, the 3α reactions start to operate more efficiently and ^{12}C production increases. However, as a result of the relatively low density in the HBS ($\rho_{\rm HBS} \lesssim 350$ g cm^{-3}), the 3α reactions do not contribute significantly to the nuclear energy generation, which is mainly the result of efficient CNO burning. The high temperatures found in the HBS also activate additional CN cycling. In particular, the chain of reactions ^{16}O(p, γ)^{17}F(β^+)^{17}O(p, γ)^{18}F(β^+)^{18}O(p, γ)^{19}F is responsible for some marginal ^{19}F production. However, the main surface enrichment in this element is the result of the subsequent deep 3DUP episodes. By the end of our computations, its surface mass fraction amounts to $X(^{19}{\rm F}) \simeq 6.4 \times 10^{-8}$, but as for ^{7}Li (see § 4), this value depends on the competitive effects resulting from its destruction by hot bottom burning (HBB) and enrichment by the 3DUP events. Note also that at the base of the HBS, the "hot" CNO cycle is operating, characterized by the main branching ^{13}N(p, γ)^{14}O(β^+)^{14}N. The NeNa and MgAl cycles are also activated and contribute locally to the production of ^{23}Na and ^{26}Al, but the abundances of these elements still remain very small ($<10^{-15}$ in mass fraction).

3.3. *The Thermally Pulsing AGB Phase*

3.3.1. *The Carbon Injection*

Thermal pulses during the AGB evolution are present in all of our models from 1.0 to 7 $M_\odot$. The occurrence of thermal pulses in zero-metallicity stars was initially investigated theoretically by Fujimoto et al. (1984). These authors first pointed out the existence of threshold values for the core mass and CNO abundances for the occurrence of thermal instabilities. In particular, they showed that if the core mass is smaller than a critical value $M^* \approx 0.73$ $M_\odot$, recurrent He shell flashes are expected to occur. They also found that for $M_{\rm core} \gtrsim M^*$, there exists a critical envelope CNO abundance ($\sim 10^{-7}$) above which He shell flashes will be triggered. The reason for this behavior was explained in Fujimoto et al. (1984) and Chieffi & Tornambé (1984) and can be summarized as follows. In massive stars, for which $M_{\rm core} \gtrsim M^*$, the lack of CNO nuclei imposes that H is burnt at very high temperatures, allowing for carbon production in the HBS. Thus, the 3α reactions are working contemporaneously in both shells and advance in mass at a similar rate. This prevents the mass growth of the intershell and thereby the occurrence of the instability. Conversely, in low-mass stars, the energy requirements are lower and the 3α reactions are not very active in the HBS. The two shells thus proceed outward at different rates—an unstable situation leading to the development of thermal pulses.

Our simulations indicate that, contrary to the theoretical expectations of Fujimoto et al. (1984), stars with

$M_{\rm core} > 0.73\ M_\odot$ do enter the thermally pulsing AGB (TP-AGB) phase. The reason for this behavior can be found in the fact that low- and intermediate-mass stars initially experience a series of instabilities (carbon injections) that progressively enrich the HBS and the envelope in heavy elements. As a consequence of this chemical "pollution," the CNO cycle operates in the HBS without the requirement of carbon production by 3α reactions, as in more metal-rich stars. The sequence of events leading to this carbon injection can be illustrated through a careful examination of our 3 $M_\odot$ model.

At the reignition of the HBS, the two burning shells are not advancing in mass at the same rate. The intershell mass increases and the HeBS is subject to small-amplitude thermal pulses. When the convective instability develops in the HeBS, it rapidly grows in mass and reaches the tail of the HBS, in a region where the H mass fraction is $X \lesssim 10^{-4}$ to 10^{-5}, and it is stopped by the large entropy barrier caused by the HBS (Iben 1976; Fujimoto 1977). As the He convective shell (HeCS) retreats, an H convective shell (HCS) forms at the H-He interface (Figs. 5 and 6). The subsequent expansion of the HCS in the underlying layers previously occupied by the pulse dredges up some carbon and initiates an H flash. During this secondary flash, the luminosity generated by the HCS ($L_{\rm H}$) reaches a maximum value of $\sim 3 \times 10^6\ L_\odot$ and greatly exceeds the He-generated luminosity. The nuclear energy production in the HCS increases very rapidly because the shell is confined to a very narrow mass range ($\Delta m_{\rm HCS} \simeq 2 \times 10^{-5}\ M_\odot$) where the temperature is on average high for proton burning ($T_{\rm HCS} \sim 95 \times 10^6$ K). As we mentioned earlier in the case of the 5 $M_\odot$ model, the luminosity of the HBS is mainly provided by the CNO cycle. However, in this model, the shell has a very low C abundance ($\sim 10^{-8}$) and the sudden ingestion of a large amount of carbon inevitably boosts the nuclear energy production.

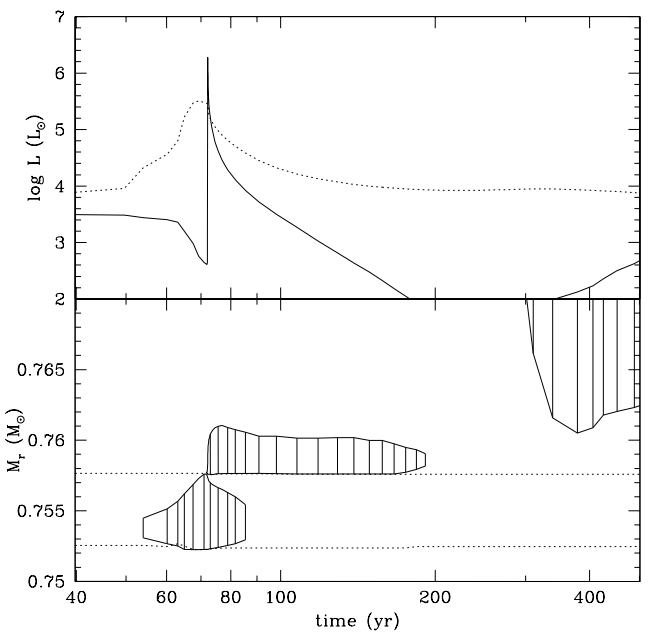

FIG. 5.—Structural evolution of the 3 $M_\odot$ model during the carbon injection (*lower panel*). The convective regions are hatched, and the dashed lines delineate the H- and He-burning regions. The dotted line inside the burning regions corresponds to the locus of maximum nuclear energy production. The upper panel shows the evolution of the H- (*solid line*) and He-generated (*dotted line*) luminosities.

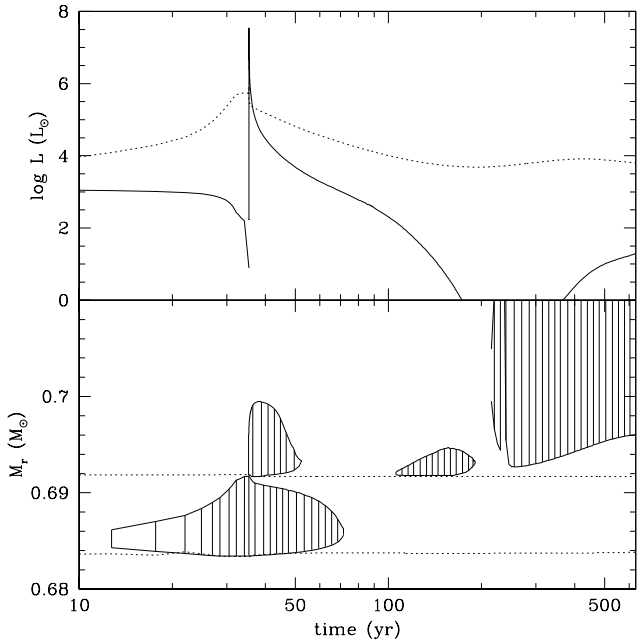

FIG. 6.—Same as Fig. 5, but for our 2 $M_\odot$ model

The energy released during the successive (He + H) flashes produces an expansion of the overlying layers that is followed by a deeper penetration of the convective envelope. In its descent, the envelope penetrates the region that was previously occupied by the HCS and enriches the surface with the elements present in the HCS. During this event, the envelope abundances of ^{12}C, ^{14}N, and ^{16}O increase significantly (see Table 3).

This irreversible process, which we call "carbon injection," is characteristic of all our intermediate-mass models, even in models with $M_{\rm core} \lesssim M^*$, and is activated only during the first thermal pulse of our 1, 1.5, 2, 4, and 5 $M_\odot$ models and during the first four instabilities in our 3 $M_\odot$ model (Fig. 5). In the latter case, the first carbon injections are not able to raise the CNO envelope abundance above the threshold value of $\sim 10^{-7}$ and the process repeats until this value is exceeded. Table 3 summarizes some properties at the end of these carbon injections. We also note that in our 7 $M_\odot$ model, the carbon enrichment of the envelope following the second dredge-up is large enough to ensure that the CNO cycle is operating efficiently inside the HBS without the need of self carbon production by 3α reactions. Therefore, this model reaches a "standard" AGB phase and the C injections are absent. C01 found that their 6 $M_\odot$ model also ended the early AGB phase with a large CNO abundance and thus, during the following evolution, behaved normally, like our 7 $M_\odot$ model. As far as our computations are concerned, carbon does not ignite in this model, a conclusion also reached by C01. This result thus indicates that the minimum mass for degenerate carbon ignition is $M_{\rm up} \geq 7\ M_\odot$. We present in Tables 4 and 5 some properties for the 7 and 3 $M_\odot$ models. Columns (1)–(13) list the following quantities: (1) the location of the HBS at the pulse ignition, (2) the location of the convective envelope relative to the HBS at the pulse ignition ($M_{\rm env} = M_{\rm H} + \Delta M_{\rm env}^{\rm H}$), (3) the pulse duration ($\Delta t_{\rm pul}$), (4) the interpulse duration ($\Delta t_{\rm inter}$ in 10^3 yr), (5) and (6) the temperature and density at the base of the pulse at the time of maximum nuclear energy genera-

TABLE 4

SELECTED PROPERTIES OF THE 7 $M_\odot$ AGB MODEL

$M_{\rm H}$ ($M_\odot$) (1)	$\Delta M^{\rm H}_{\rm env}$ ($10^{-3}\,M_\odot$) (2)	$\Delta t_{\rm pul}$ (yr) (3)	$\Delta t_{\rm inter}$ (10^3 yr) (4)	$T^{\rm max}_{\rm pul}$ (10^8 K) (5)	$\rho^{\rm max}_{\rm pul}$ (cgs) (6)	$L^{\rm max}_{\rm He}$ ($L_\odot$) (7)	$\Delta M^{\rm H}_{\rm pul}$ ($10^{-3}\,M_\odot$) (8)	$M_{\rm pul}$ ($10^{-3}\,M_\odot$) (9)	$\Delta M_{\rm DUP}$ ($10^{-3}\,M_\odot$) (10)	Surface Mass Fraction		
										^{12}C (11)	^{14}N (12)	^{16}O (13)
1.0557	0.0800	2.25	0.8081	2.278	1297.	7.244 (4)	0.4341	0.263	0.0513	1.270 (−6)	2.622E−05	9.519 (−8)
1.0559	0.0533	4.39	0.9787	2.367	1397.	9.395 (4)	0.2687	0.385	0.0391	1.103 (−6)	2.649E−05	9.852 (−8)
1.0562	0.0444	4.97	1.0196	2.494	1459.	1.437 (5)	0.1955	0.484	0.0148	1.131 (−6)	2.644E−05	1.041 (−7)
1.0565	0.0209	6.70	1.1066	2.565	1609.	2.005 (5)	0.1471	0.532	0.0069	1.179 (−6)	2.636E−05	1.113 (−7)
1.0568	0.0179	5.56	1.0775	2.628	1599.	2.537 (5)	0.1305	0.543	0.0029	1.191 (−6)	2.634E−05	1.195 (−7)
1.0571	0.0129	5.29	0.9974	2.674	1810.	3.106 (5)	0.1157	0.550	−0.0002	1.213 (−6)	2.630E−05	1.271 (−7)
1.0574	0.0122	4.82	0.9392	2.783	1599.	3.429 (5)	0.1044	0.583	−0.0012	1.237 (−6)	2.626E−05	1.335 (−7)
1.0577	0.0129	5.02	0.9436	2.747	1813.	4.094 (5)	0.0933	0.557	0.0001	1.251 (−6)	2.623E−05	1.384 (−7)
1.0584	0.0174	4.05	1.2463	2.901	1824.	7.483 (5)	0.0707	0.600	−0.0029	1.277 (−6)	2.619E−05	1.458 (−7)
1.0587	0.0165	4.33	1.2892	2.929	1869.	8.776 (5)	0.0600	0.600	−0.0018	1.307 (−6)	2.614E−05	1.479 (−7)
1.0590	0.0167	4.14	1.3120	2.936	1940.	9.615 (5)	0.0574	0.586	−0.0034	1.314 (−6)	2.613E−05	1.491 (−7)
1.0594	0.0149	4.50	1.3704	2.960	1734.	9.870 (5)	0.0546	0.567	−0.0050	1.330 (−6)	2.611E−05	1.495 (−7)
1.0597	0.0149	3.87	1.3747	3.001	1784.	1.222 (6)	0.0509	0.578	−0.0042	1.342 (−6)	2.609E−05	1.495 (−7)
1.0601	0.0153	4.34	1.4901	3.057	1961.	1.581 (6)	0.0446	0.602	−0.0028	1.356 (−6)	2.607E−05	1.493 (−7)
1.0604	0.0142	4.33	1.7442	3.094	2745.	2.116 (6)	0.0375	0.669	−0.0833	1.388 (−6)	2.602E−05	1.487 (−7)
1.0608	0.0147	4.11	2.0434	3.202	2822.	3.848 (6)	0.0292	0.771	−0.1142	1.561 (−6)	2.876E−05	1.905 (−7)
1.0611	0.0147	4.11	2.5918	2.955	3055.	6.657 (6)	0.0250	0.878	−0.3037	1.910 (−6)	3.515E−05	3.094 (−7)
1.0613	0.0121	4.46	2.3100	3.300	3019.	6.254 (6)	0.0238	0.815	−0.1720	3.186 (−6)	5.996E−05	1.049 (−6)
1.0615	0.0118	4.12	2.2375	3.120	4184.	2.763 (7)	0.0155	0.518	−0.1289	3.981 (−6)	7.567E−05	1.414 (−6)
1.0618	0.0111	4.59	...	3.246	4238.	9.356 (6)	0.0193	0.897	...	4.090 (−6)	7.838E−05	1.067 (−6)

TABLE 5

SELECTED PROPERTIES OF THE 3 $M_\odot$ AGB MODEL

$M_{\rm H}$ ($M_\odot$) (1)	$\Delta M^{\rm H}_{\rm env}$ ($10^{-3}\,M_\odot$) (2)	$\Delta t_{\rm pul}$ (yr) (3)	$\Delta t_{\rm inter}$ (10^3 yr) (4)	$T^{\rm max}_{\rm pul}$ (10^8 K) (5)	$\rho^{\rm max}_{\rm pul}$ (cgs) (6)	$L^{\rm max}_{\rm He}$ ($L_\odot$) (7)	$\Delta M^{\rm H}_{\rm pul}$ ($10^{-3}\,M_\odot$) (8)	$M_{\rm pul}$ ($10^{-3}\,M_\odot$) (9)	$\Delta M_{\rm DUP}$ ($10^{-3}\,M_\odot$) (10)	Surface Mass Fraction		
										^{12}C (11)	^{14}N (12)	^{16}O (13)
0.7576[a]	21.6866	139.83	27.63	2.339	2209.	3.227 (5)	0.1494	5.237	2.8497	9.63 (−17)	1.09 (−14)	3.06 (−16)
0.7604[a]	8.4066	92.25	27.09	2.691	1821.	5.926 (6)	0.0707	5.502	1.0034	2.65 (−11)	6.91 (−10)	5.59 (−12)
0.7619[a]	13.2376	150.31	15.18	2.513	2389.	6.251 (5)	0.0612	4.659	1.0784	5.69 (−11)	2.247 (−9)	2.29 (−11)
0.7653[a]	10.1281	65.31	30.03	2.573	1065.	1.628 (6)	0.0819	5.311	2.2147	4.95 (−10)	1.814 (−8)	1.92 (−10)
0.7683	2.4285	66.12	30.98	2.802	1780.	1.208 (7)	0.0972	6.045	−0.0205	2.071 (−7)	9.312 (−8)	1.846 (−6)
0.7713	2.1531	31.00	30.81	2.867	1780.	1.568 (7)	0.0684	5.986	−0.0351	2.070 (−7)	9.367 (−8)	1.845 (−6)
0.7742	1.9328	26.61	30.75	2.913	1896.	1.773 (7)	0.0656	5.696	−0.0378	2.070 (−7)	9.408 (−8)	1.845 (−6)
0.7772	1.7731	24.67	29.40	2.933	1804.	2.270 (7)	0.0545	5.540	−0.0433	2.069 (−7)	9.447 (−8)	1.845 (−6)
0.7802	1.6224	21.39	28.32	2.977	1951.	2.407 (7)	0.0454	5.290	−0.0454	2.069 (−7)	9.484 (−8)	1.844 (−6)
0.7830	1.5284	21.96	27.39	2.984	1937.	2.367 (7)	0.0522	5.051	−0.0476	2.068 (−7)	9.519 (−8)	1.844 (−6)
0.7857	1.4341	21.38	26.45	2.989	1830.	2.503 (7)	0.0485	4.888	−0.0485	2.068 (−7)	9.554 (−8)	1.844 (−6)
0.7884	1.3783	17.46	27.81	2.984	1774.	2.381 (7)	0.0593	4.723	−0.0473	2.068 (−7)	9.588 (−8)	1.843 (−6)
0.7912	1.3000	33.41	35.25	3.027	1851.	2.827 (7)	0.0519	4.702	−0.0641	2.067 (−7)	9.621 (−8)	1.843 (−6)
0.7944	0.8771	26.09	42.44	3.137	1930.	6.745 (7)	0.0133	5.150	−0.3435	1.299 (−6)	2.402 (−7)	3.836 (−6)
0.7983	0.3438	26.79	45.46	3.278	2142.	2.256 (8)	0.0118	6.027	−1.0055	2.274 (−5)	3.122 (−7)	2.333 (−5)
0.8020	0.1770	39.25	47.20	3.412	2566.	4.126 (8)	0.0173	6.446	−1.4912	1.245 (−4)	3.152 (−7)	4.265 (−5)
0.8054	0.1085	34.24	48.09	3.469	2653.	6.075 (8)	0.0171	6.624	−1.8280	2.949 (−4)	3.249 (−7)	5.269 (−5)
0.8087	0.0705	49.59	48.51	3.564	3090.	7.975 (8)	0.0164	6.725	−2.1434	5.091 (−4)	3.662 (−7)	5.875 (−5)
0.8118	0.0781	61.04	55.31	3.612	3186.	1.045 (9)	0.0111	6.806	−2.3621	7.081 (−4)	1.269 (−5)	6.474 (−5)
0.8150	0.0697	57.29	122.18	3.683	3371.	1.591 (9)	0.0112	7.088	−3.4720	3.712 (−4)	6.690 (−4)	7.148 (−5)
0.8190	0.0120	87.99	150.48	3.908	3999.	7.121 (9)	0.0135	8.735	−4.9227	5.190 (−5)	1.670 (−3)	7.992 (−5)
0.8226	0.0101	65.82	130.23	3.956	3832.	1.496 (10)	0.0082	9.586	−7.1713	7.372 (−5)	2.400 (−3)	9.216 (−5)
0.8240	0.0074	66.75	...	4.054	4443.	1.753 (10)	0.0111	9.729	...	1.031 (−4)	3.261 (−3)	1.046 (−4)

[a] Carbon injection episodes.

tion, (7) the peak luminosity of the pulse, (8) the location of the top of the convective pulse relative to the HBS ($M_{\rm pul}^{\rm top} = M_{\rm H} - \Delta M_{\rm pul}^{\rm H}$), (9) the pulse mass ($M_{\rm pul} = M_{\rm pul}^{\rm top} - M_{\rm pul}^{\rm bot}$), (10) the location of the deepest penetration of the convective envelope relative to HBS after the pulse ($M_{\rm env}^{\rm min} = M_{\rm H} + \Delta M_{\rm DUP}$), and the surface mass fractions of (11) ^{12}C, (12) ^{14}N, and (13) ^{16}O at the time of pulse ignition.

We also find that after the disappearance of the HCS and before the envelope penetrates the region polluted by the HCS, a secondary convective zone can develop at the border of the H-rich region. This feature, illustrated in Figure 6 in the 2 $M_\odot$ model, depends on the mesh resolution and numerical scheme (see below). Although this secondary convective shell never mixes with the underlying ^{12}C- and ^{4}He-rich layers, this situation is unstable with respect to the Schwarzschild criterion because of the large positive value of $\nabla_{\rm rad} - \nabla_{\rm ad}$ at the bottom of the convective region (e.g., Castellani, Gianone, & Renzini 1971a, 1971b). When $\nabla_{\rm rad} > \nabla_{\rm ad}$, any perturbation of the convective boundary would give rise to extra mixing, and in particular carbon could be injected into the convective zone with the possible triggering of a new H flash and further chemical contamination of the envelope. The formation of a "secondary convective shell" above the H discontinuity has also been found by Dominguez et al. (2000), after nine weak instabilities during the evolution of a 5 $M_\odot$ primordial star, and it strikingly resembles the one depicted here except that in their simulation it takes place before the C injection (see their Fig. 7). Finally note that in our simulations this feature, if real, has no influence on the subsequent evolution since it does not mix with the underlying C-rich layers.

The existence of C injection episodes at the beginning of the AGB phase has recently been found by C01 in their computations of zero-metallicity intermediate-mass stars. In these computations, this process follows the same course of events: a convective shell develops at the base of the H-rich layer, ingests carbon, and initiates an H flash. The additional energy released by this H flash subsequently leads to a deeper penetration of the convective envelope that reaches the CNO-enriched HCS and pollutes the envelope. Our results thus confirm these independent computations and the unusual circumstances by which primordial stars enter the TP-AGB phase.

Finally, we would like to discuss briefly the sensitivity of the results to the numerical treatment. During the penetration of the He-driven convective zone into the H-rich layers and subsequent carbon injection event, we performed numerous tests, adopting different time steps and different mass zoning. In these tests, we also accounted or not for a small overshooting characterized by $d = 0.05H_P$. Our numerical experiments indicate that when extra mixing at the borders of the convective shells is allowed, the penetration of the HCS in the underlying C-rich layer is present in all the models, irrespective of the mesh point and time stepping. However, when overshooting is not included, the C injection then depends on the spatial and temporal resolution. We also report that in some cases a secondary convective zone develops just above the H-He discontinuity, as previously reported and shown in Figure 6. The appearance of this feature is, however, arbitrarily dependent on the adopted temporal and spatial resolutions. The amplitude of the H flash and the extent of the HCS vary slightly from one computation to another. In particular, adopting a larger time step leads in general to a larger value of $L_{\rm H}$ at its maximum, which is the opposite effect of having a more refined mesh. As a consequence of these numerical uncertainties, the envelope chemical composition after the dredge-up event may vary by a factor of a few. The stronger the H flash, the deeper the convective envelope plunges and the higher is the surface metallicity. While these differences appear to be relatively large, we have to remember that the envelope composition of the stars that experience these C injections is almost devoid of metals. Therefore, a small difference in the dredge-up mass can lead to significant changes after the mixing events. Basically, it is much easier to raise the metallicity from almost zero to $\sim 10^{-6}$ than from 10^{-6} to 10^{-5}. The important point for the subsequent evolution is that a substantial amount of carbon has been deposited into the envelope. Remembering that an envelope mass fraction of ^{12}C as low as $X_{^{12}{\rm C}} \simeq 10^{-7}$ is sufficient to switch H burning to the CNO cycle, we realize that an uncertainty in the amount of C dredged up in the envelope by as much as an order of magnitude will not result in a change in the subsequent evolution because the C injection has already raised the ^{12}C abundance well above this limit. The influence on the yields will also be negligible since the main chemical enrichment of the surface comes from the 3DUP event. As a conclusion, even though the modeling of this mixing phase suffers from some numerical uncertainties, its occurrence is well established from our simulations and those of C01, and we are confident that the exact modeling of this process does not influence the subsequent evolution of the TP-AGB stars substantially.

3.3.2. *The Degenerate Pulses*

Our 4 and 5 $M_\odot$ models exhibit a different kind of thermal pulse, which we refer to as "degenerate pulses" following the designation given by Frost, Lattanzio, & Wood (1998b). We illustrate their characteristics by returning to the evolution of our 5 $M_\odot$ model.

After a series of 12 weak instabilities, the 5 $M_\odot$ model finally undergoes the carbon injection described previously. After $\sim$15,800 yr, a standard thermal pulse takes place. Because of the relatively high degeneracy in the He shell, this second pulse ignites very deeply (at $M_r \simeq 0.901\ M_\odot$) and gives rise to a very extended convective region. The helium-generated luminosity reaches $L_{\rm He} \simeq 1.5 \times 10^7\ L_\odot$ at its peak and is maintained above $10^3\ L_\odot$ for $\approx$2900 yr, which allows for an efficient He depletion in the intershell.

Following the pulse, the convective envelope deepens and produces a dredge-up characterized by $\lambda \sim 0.4$, where $\lambda = \Delta M_{\rm DUP}/\Delta M_{\rm H}$ represents the ratio of the mass that has been dredged up ($\Delta M_{\rm DUP}$) to the mass advance of the HBS between the last 3DUP and the beginning of the pulse ($\Delta M_{\rm H}$). During the subsequent interpulse, HBB starts operating and leads temporarily to the production of ^{7}Li as a result of the Cameron-Fowler (1971) mechanism. It also increases the surface abundances of ^{13}C and ^{14}N at the expense of ^{12}C. After $\simeq$14,000 yr, a stronger instability is triggered in the HeBS ($L_{\rm He} \simeq 5 \times 10^7\ L_\odot$) and a deep 3DUP ensues ($\lambda \sim 0.7$), which rapidly extinguishes the instability. This quick deactivation of the third pulse (in $\sim$10 yr) does not allow for a large depletion of the helium present in the intershell convective tongue, and a long tail of unburnt He ($Y \lesssim 0.1$) is left behind the pulse (Fig. 7, *lower panel*). When this He tail reignites after $\sim$70 yr, a second convective instability develops (Fig. 8). It lasts for $\sim$40 yr and generates a

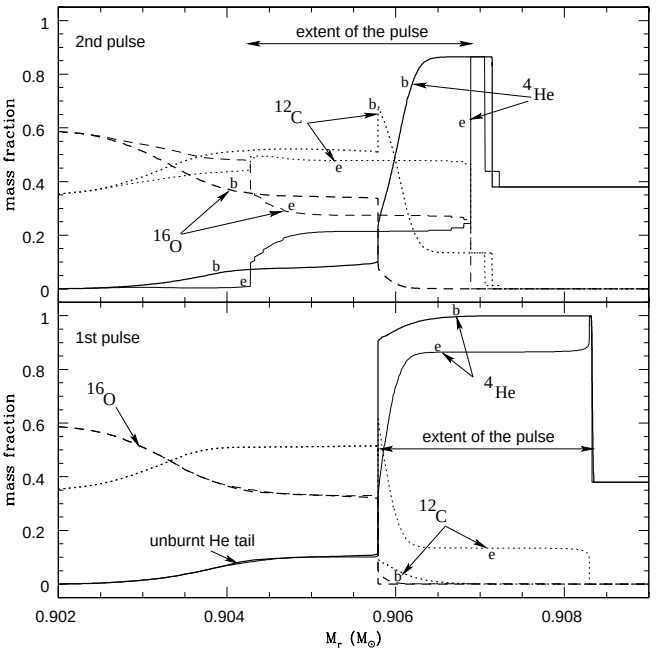

FIG. 7.—Abundance profiles in mass fraction of ^{4}He (*solid line*), ^{12}C (*dotted line*), and ^{16}O (*dashed line*) during the degenerate pulse of our 5 $M_\odot$ model. In the lower and upper panels, the thick and thin lines correspond to the beginning ("b") and the end ("e") of the pulses and are separated in time by 10 and 40 yr, respectively. Note the large amount of He remaining in the intershell and long tail of unburnt He left after the first pulse.

nuclear luminosity of $L_{\rm He} \sim 10^6\ L_\odot$. At the end of this secondary pulse, the He tail has disappeared and a large fraction of the He present in the intershell has also been burnt (Fig. 7, *upper panel*). We also found a degenerate pulse in our 4 $M_\odot$ model (Fig. 8). Its characteristics are very similar: the maximum He-generated luminosities during each instability are $L_{\rm He} \simeq 8 \times 10^6$ and $8 \times 10^5\ L_\odot$, respectively, slightly lower than in the 5 $M_\odot$ model, and the durations of the two convective pulses are ~30 and 60 yr. We note, however, that in the 4 $M_\odot$ case the two instabilities are separated in time by only ~10 yr and look like a failed pulse.

This phenomenon is very similar to the one described in detail by Frost et al. (1998b), who first reported the appearance of the so-called degenerate thermal pulses in their computation of a low-metallicity ($Z = 0.004$) 5 $M_\odot$ AGB model. The occurrence of these instabilities results from the fact that the star experiences a deep dredge-up that quenches rapidly the instability, preventing an efficient He depletion in the intershell. It is also favored by a higher degeneracy that prevents efficient helium burning because of the lower temperature found at the base of the pulse. We present in Figure 9 the evolution of the degeneracy parameter η and temperature, before and after the standard pulse preceding the degenerate instability, during the He accretion phase and just before the ignition of the (degenerate) pulse. As shown, the degeneracy is lifted during the pulse and the temperature increases in the intershell region (*solid and dotted lines*). During the He accretion phase, η increases and the temperature excess dissipates (*short-dashed line*). Finally, when the degenerate pulse develops, the parameter η is larger and the temperature lower than in the previous pulse. However, contrary to Frost et al. (1998b), our degenerate pulse develops very early in the TP-AGB phase, probably as a result of the higher degeneracy of our zero-metallicity stars. We also note that the amplitude of the generated luminosity and amount of dredge-up before the pulse are smaller in our simulations. These calculations are totally independent of those of Frost et al. (1998b), and they verify that degenerate pulses indeed occur (at least in models, if not in real stars!).

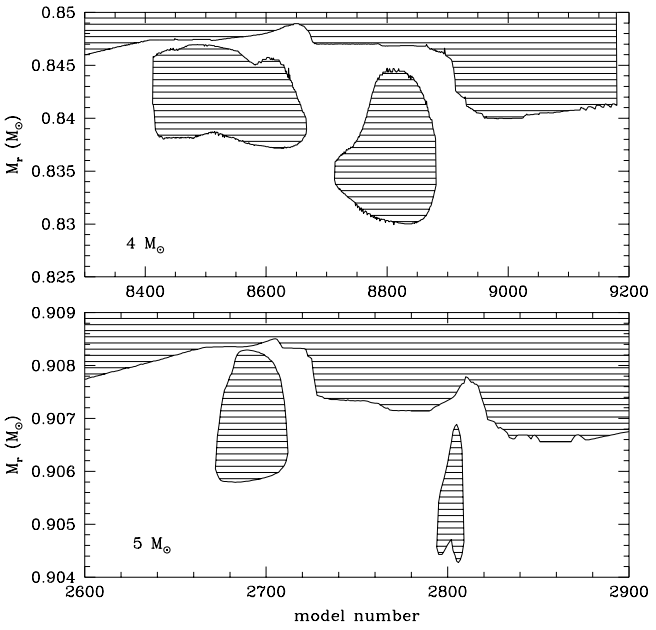

FIG. 8.—Convective zones as a function of model number for the degenerate pulses in the 4 and 5 $M_\odot$ models.

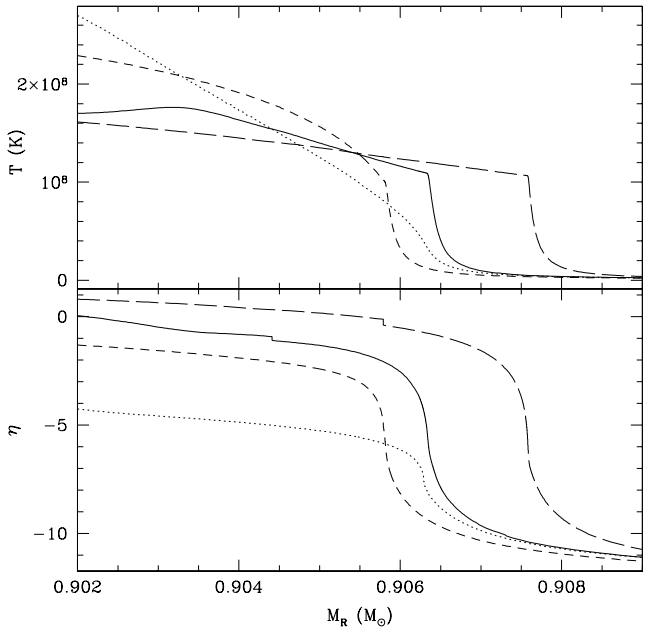

FIG. 9.—Evolution of the profiles of temperature and degeneracy parameter η in the 5 $M_\odot$ model. The solid and dotted lines correspond to the beginning and end of the pulse preceding the degenerate pulse, respectively. The short- and long-dashed lines depict the situation during the He accretion phase and at the beginning of the degenerate pulse, respectively. Note the higher degeneracy and lower temperature at the ignition of the latter pulse. [*See the electronic edition of the Journal for a color version of this figure.*]

After this series of events, our 4 and 5 $M_\odot$ stars enter a "standard" AGB evolution phase. We note, however, that the temperature and degeneracy keep increasing at the base of the helium shell. This situation is favorable for a later development of a degenerate pulse (see also Frost et al. 1998b). Finally, note that C01 do not report any "strange" behavior such as the one described here in the evolution of their 5 $M_\odot$ $Z = 0$ model.

3.3.3. *Nucleosynthesis*

When the temperature in the convective pulse exceeds $\sim 3 \times 10^8$ K, as is found in some late thermal pulses or in more massive stars like in the 5 $M_\odot$ model, a large number of neutrons are released via the reaction ^{22}Ne(α, n)^{25}Mg. As an example, during the 17th pulse of our 3 $M_\odot$ model, at the peak of neutron production, the neutron density $N_n > 3 \times 10^{10}$ cm^{-3} everywhere in the pulse and reaches a value of $N_n \simeq 10^{13}$ cm^{-3} at the base of the convective instability where $T \simeq 3.9 \times 10^8$ K. At lower temperatures, a marginal source of neutrons is provided by the ^{13}C(α, n)^{16}O chain of reaction, the ^{13}C coming initially from the ashes of the HBS. These neutrons mainly react with the ^{14}N and some ^{14}C is produced, which in turn reacts with α-particles leading to ^{18}O production and then by another α-capture to the formation of ^{22}Ne. The ^{22}Ne is also subject to (α, γ) and (α, n) reactions, and the abundances of ^{26}Mg and ^{25}Mg are increased, respectively. Note that after the rapid depletion of ^{14}N, some ^{13}C is produced by ^{12}C(n, γ) (see Table 6).

Further neutron captures on ^{22}Ne and ^{26}Mg increase the ^{23}Na and ^{27}Al abundances, respectively, and after the bottleneck formed by ^{33}S(n, α)^{30}Si is passed, neutron captures can proceed on heavier elements (see Goriely & Siess 2001 for more details). Some ^{19}F is also synthesized by ^{18}O(p, α)^{15}N(α, γ)^{19}F. In the inner region, ^{12}C continues to be produced via the 3α reactions and is partly destroyed by α-capture to produce ^{16}O. In the upper part of the pulse, the largest nuclear fluxes result from proton captures on ^{12}C, ^{14}N, ^{16}O, and ^{18}O, the protons mainly supplied by ^{14}N(n, p)^{14}C. We also found that the chain of ^{16}O(n, γ)^{17}O(α, n)^{20}Ne contributes to the buildup of ^{20}Ne, while restoring a substantial number of neutrons. The abundances of some key elements inside selected thermal pulses of our 3 $M_\odot$ model are presented in Table 6.

Finally, the main reactions that take place in the HCS are the CNO reactions. The fact that the elements synthesized during the pulse are mixed in the HCS at relatively high temperatures also leads, but to a much lesser extent, to marginal α-capture on CNO isotopes. However, because of the small abundance of Ne and Mg in the HCS, the NeNa and MgAl cycles are not working efficiently.

3.3.4. *The Occurrence of Dredge-up Episodes*

3DUP episodes are responsible for the formation of carbon stars (see, e.g., Iben & Renzini 1982) and are also necessary (but not sufficient) to account for the synthesis and observations of *s*-process elements in AGB stars. However, details of 3DUP are dependent on numerous factors, such as the numerical scheme (e.g., Frost & Lattanzio 1996), the spatial or temporal resolution of the simulations (Straniero et al. 1997), and the input physics (choice of opacity, mass-loss rate), and are favored by the presence of extra mixing or overshooting. In past years, new formalisms for overshooting (e.g., Herwig et al. 1997) and rotationally induced mixing (Langer et al. 1999) have been developed in order to facilitate the occurrence of 3DUP to address the issues related to the luminosity function of carbon stars (so-called C star mystery) and production of *s*-process elements.

The 3DUP is characterized by the penetration of the convective envelope into a region of significantly different chemical composition, and as a consequence, a discontinuity in $\nabla_{\rm rad} - \nabla_{\rm ad}$ appears at the inner convective boundary. As described previously, this situation is unstable and favors convective overshoot from the envelope into the underlying layers. To account for this natural tendency of the convective envelope to cross the strict limit defined by the Schwarzschild criterion, we have allowed for a small overshooting characterized by $d = 0.05 H_P$. In this context we were able to reproduce the 3DUP, and by the end of our computations it is present in all of our models with $1.5 \lesssim M \lesssim 7$ $M_\odot$. It starts operating at the first (degenerate) pulse of our 4 and 5 $M_\odot$ stars and is characterized by relatively large initial values of $\lambda \geq 0.7$. In the 2, 3, and 7 $M_\odot$ models the 3DUP comes into play at the 6th, 9th, and 15th pulses, respectively (Figs. 10, 11, and 12). Note that C01 also find 3DUP events in their 7 $M_\odot$ model after the 13th or 14th pulse, depending on their prescription for extra mixing ($\beta = 0.005$ and 0.01, respectively). At the termination of our computations, the 1 $M_\odot$ model has undergone two deep mixing events during the 4th and 8th pulses (Fig. 13), but we suspect that these may be artifacts due to a smaller spatial resolution at that time. Finally, we report that in the 1.5 $M_\odot$ model the 3DUP follows the first convective instability. The evolution of the latter star is peculiar in the sense that it develops extremely strong pulses ($L_{\rm He} \sim 10^8$–10^9 $L_\odot$) since the beginning of the TP-AGB phase. This behavior is certainly related to the higher degeneracy of the He layers in this model, whose mass lies close to the upper mass limit for degenerate He core ignition. As a consequence of the higher degeneracy, the pulses are stronger and the convective penetration deeper. Inspection of the structure indicates that the extent of the convective instabilities is much larger than in

TABLE 6

MASS FRACTIONS OF SOME ELEMENTS INSIDE SELECTED THERMAL PULSES OF THE 3 $M_\odot$ MODEL

Pulse[a]	^{13}C	^{14}C	^{14}N	^{22}Ne	^{23}Na	^{25}Mg	^{26}Mg	^{27}Al	^{30}Si	^{36}S
2.....	1.26 (−9)	2.05 (−7)	6.43 (−6)	1.30 (−2)	8.80 (−5)	1.36 (−4)	4.08 (−4)	9.16 (−4)	3.55 (−3)	5.32 (−4)
2.....	4.36 (−9)	3.37 (−8)	5.1 (−13)	7.36 (−3)	4.66 (−5)	1.43 (−4)	2.80 (−4)	4.63 (−4)	1.96 (−3)	2.67 (−4)
10.....	1.7 (−12)	1.43 (−6)	7.21 (−5)	8.02 (−4)	5.66 (−6)	8.45 (−6)	1.80 (−5)	3.21 (−5)	3.92 (−7)	6.69 (−7)
10.....	3.4 (−11)	3.63 (−5)	1.30 (−9)	9.40 (−4)	1.79 (−5)	2.38 (−5)	6.47 (−5)	1.31 (−4)	1.85 (−6)	1.61 (−6)
17.....	4.7 (−11)	8.35 (−7)	1.98 (−4)	4.30 (−4)	4.16 (−6)	3.04 (−5)	1.05 (−4)	3.91 (−6)	4.75 (−7)	1.37 (−8)
17.....	1.4 (−12)	9.9 (−11)	1.9 (−13)	9.27 (−4)	3.22 (−5)	3.55 (−4)	1.37 (−3)	2.82 (−5)	2.76 (−6)	7.49 (−8)

NOTE.—The abundances are shown near the beginning and end of the convective pulse.

[a] The pulse number is counted after the end of the carbon injection episodes. Details about the evolution of this model are provided in Table 5.

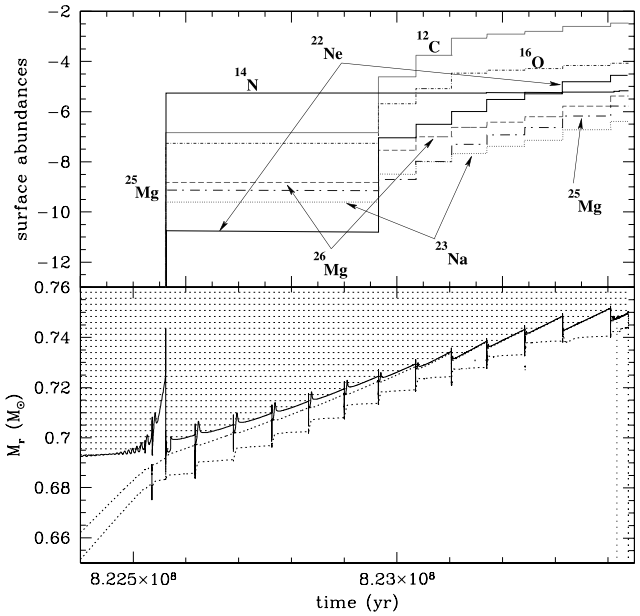

FIG. 10.—*Lower panel:* Evolution of the structure of the 2 $M_\odot$ model. The dotted region represents the convective envelope, and the dashed lines represent the locus of maximum energy generation by the HBS and HeBS. *Upper panel:* Surface abundances (in mass fraction) of ^{12}C, ^{16}O, ^{14}N, ^{22}Ne, ^{23}Na, ^{26}Mg, and ^{25}Mg. [*See the electronic edition of the Journal for a color version of this figure*.]

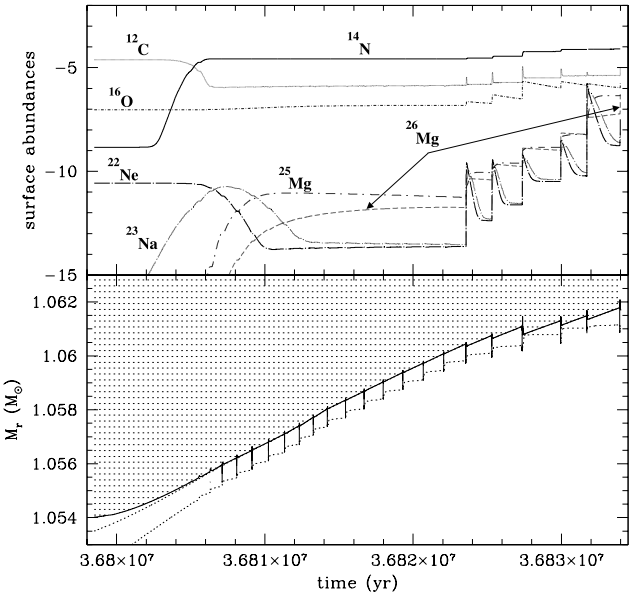

FIG. 12.—Same as Fig. 10, but for our 7 $M_\odot$ model. Note the rapid depletion of ^{23}Na by proton captures due to the high temperature at the base of the convective envelope ($T \sim 10^8$ K). [*See the electronic edition of the Journal for a color version of this figure*.]

the two adjacent mass tracks (1 and 2 $M_\odot$) and also that the pulse ignites near the base of the convective instability. The impact of the 3DUP on the surface abundances is discussed in § 4.

4. CHEMICAL EVOLUTIONARY CONSEQUENCES

One of the great interests in the first generation of stars is their effect on the chemical evolution of the universe. We have seen that these stars do indeed experience the 3DUP on the AGB, as well as HBB. The consequences of these events for the chemical history of the universe are our concern in this section.

The largest uncertainties in calculating the chemical yields are the unknown mass-loss history of the stars and the amount of dredge-up material that affects both the chemical composition and the efficiency at which stellar matter is returned to the interstellar medium. If, as is believed, the mass loss in low- and intermediate-mass stars

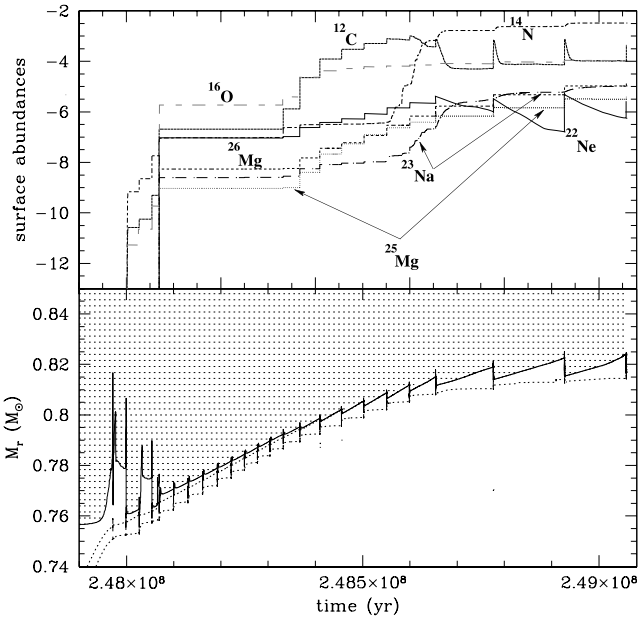

FIG. 11.—Same as Fig. 10, but for our 3 $M_\odot$ model. Note the large production of ^{14}N and ^{23}Na due to efficient HBB. [*See the electronic edition of the Journal for a color version of this figure*.]

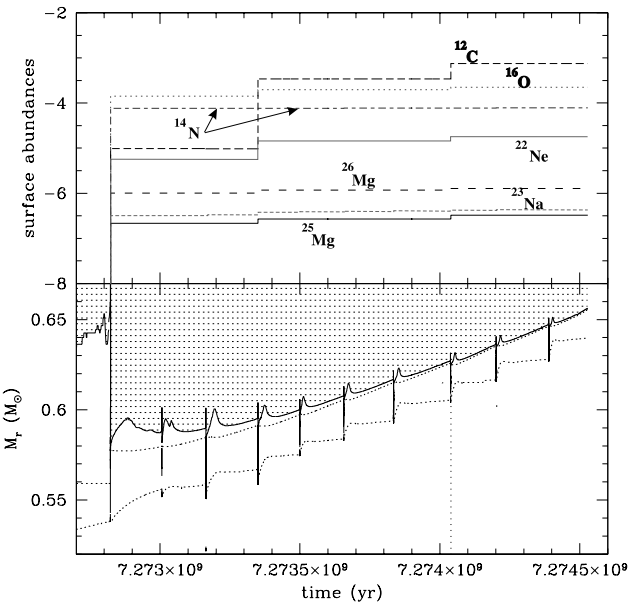

FIG. 13.—Same as Fig. 10, but for our 1 $M_\odot$ model. Note that dredge-up only occurs in the 4th and 8th pulses. [*See the electronic edition of the Journal for a color version of this figure*.]

is driven by (or at least strongly coupled to) radiation pressure on grains, then an envelope free from grains could have a very reduced mass loss. However, if the 3DUP takes place, as found in these simulations, the envelope is enriched in metals (mainly C, N, and O) and the mass loss is switched on, although later in the evolution compared to higher metallicity stars. Thus, the initial-final mass relation is likely to favor the production of more massive white dwarfs at $Z = 0$ than for other values of metallicity. On the other hand, the higher effective temperatures characteristic of these stars might make it more difficult for grains to form (even though nova systems show that grains form even in unlikely environments). As a consequence, the uncertainty in the form of both the mass-loss rate and the efficiency of the 3DUP is still a major limitation at present and prevents us from calculating yields for our models.

Prior to the AGB phase, the only significant consequence of the (second) dredge-up is the increase in helium abundance. But as we have noted above, all of our models do experience the 3DUP. This is a major source of ^{12}C, of course, but also of other species. For example, the ^{12}C is processed by the HBS and the CN cycle thus produces ^{14}N. When this ^{14}N is exposed to high temperatures and a significant flux of α-particles during the next thermal pulse, it is completely burned into ^{22}Ne. The ^{22}Ne is, in turn, partially burned by further α-captures into ^{25}Mg [if subject to (α, n) reactions] or ^{26}Mg [if subject to (α, γ) instead]. Details depend on the stellar mass, of course, as the main parameter determining the shell temperatures, but we expect both to occur to some extent.

We have also seen that for masses above about 2 $M_{\odot}$ there is activation of HBB. This is in distinct contrast to the standard assumption in the literature that the minimum mass for HBB is between 4 and 5 $M_{\odot}$. Although this is true for solar metallicity, a decrease in Z will cause the onset of HBB to occur at lower masses, as found in Lattanzio et al. (2001). Clearly these stars will be significant sources of ^{14}N in the early universe (see top panel of Figs. 10, 11, 12, and 13).

However, HBB does more than burn ^{12}C into ^{14}N. It will also process the ^{22}Ne into ^{23}Na, as well as the ^{25}Mg and ^{26}Mg into ^{26}Al and ^{27}Al, respectively. A potentially important reaction is the production of ^{7}Li via the Cameron-Fowler mechanism. But although ^{7}Li is rapidly and abundantly produced by HBB, it is also destroyed on subsequent passes through the bottom of the convective envelope. Hence, the Li-rich phase is only temporary. Whether these stars can add to the initial Li abundance in the early universe will depend crucially on the mass loss involved: if the mass loss is significant while the surface Li abundance is high, then they will produce a large Li yield. If, however, the Li is depleted before the high mass-loss rates begin (a situation believed to occur in the current generation of stars), then the yields will be negligible or even negative. The reader is referred to Travaglio et al. (2001) for a fuller discussion.

Figures 10, 11, 12, and 13 depict the evolution of the structure concomitantly to the evolution of the surface abundances of some keys elements. As can be seen, during the initial carbon ingestion, the stars soon become N-rich as a consequence of dredging up to the surface the products of the CNO cycle that was operating in the HCS. Following a few thermal pulses, the 3DUP takes place and the abundances of C, O, Mg, Ne, and Na increase. Note that the stars rapidly become C-rich. However, it is not clear whether primordial stars will maintain their large C/O ratio or not. Indeed, the evolution of the C/O ratio depends on the competition between 3DUP (which increases the C abundance) and HBB (which destroys it), which in turn depends on the envelope mass, i.e., on mass loss. Frost et al. (1998a) showed that, as the envelope mass decreases, HBB shuts down first while 3DUP continues. As far as our computations are concerned, our low- and intermediate-mass stars show a C/O ratio larger than 1, but for how long this feature will be maintained is presently unknown. When the temperatures at the base of the convective envelope approach 4.0×10^7 K, HBB is activated. In the 3 and 7 $M_{\odot}$ models, the signatures of this efficient nuclear burning are well illustrated: the ^{12}C is rapidly converted into ^{14}N, which becomes the most abundant metal in the envelope, and the ^{22}Ne after proton capture produces a large amount of ^{23}Na. However, because of the maintenance of a high temperature at the base of the convective envelope ($T \gtrsim 10^8$ K, $\rho > 10$ g cm^{-3}) of the 7 $M_{\odot}$ model, proton captures on ^{23}Na destroy this element at the benefit of ^{20}Ne and ^{24}Mg.

Finally, if mixing of protons is taking place at the base of the convective envelope (e.g., as a result of diffusive overshooting), the protons will react on the abundant ^{12}C and form a "^{13}C pocket," which will be responsible for a large release of neutrons (Iben & Renzini 1982; Busso, Gallino, & Wasserburg 1999). The neutrons will then be captured by the most abundant nuclei, i.e., C, N, O, and Ne, and lead to *s*-process enrichment *despite* the absence of iron (Goriely & Siess 2001). As a consequence, we can expect *s*-process elements to have formed in primordial stars.

4.1. *Conclusions*

The evolution of low- and intermediate-mass stars in the mass range $1 \lesssim M \leq 5$ $M_{\odot}$ is characterized by the development of mixing episodes at the beginning of the AGB phase. During these events, a secondary convective shell develops at the H-He discontinuity, expands, and overlaps with the underlying carbon-rich layers left by the receding pulse. The engulfed carbon initiates an H flash, which further expands the structure and produces a deeper penetration of the envelope. The envelope eventually reaches the region previously occupied by this secondary shell, and CNO catalysts are dredged up to the surface by the carbon injection mechanism.

This mechanism then allows low- and intermediate-mass stars to successfully achieve the thermally pulsating phase. These results confirm recent similar findings by C01. Assuming a small degree of overshooting at the base of the convective envelope, we find that a 3DUP rapidly takes place and that HBB is already active in stars with $M \gtrsim 2$ $M_{\odot}$. These processes contribute to significant surface enrichment in ^{14}N (which is further enhanced by HBB), ^{16}O, ^{12}C (but the latter is partially destroyed by HBB), and ^{4}He with possible Mg pollution. Primordial AGB stars are also found to be a potential site for *s*-process nucleosynthesis, despite the absence of iron seeds (Goriely & Siess 2001; Busso et al. 2001)

The metal enrichment of the envelope activates mass loss, although later in the evolution compared to higher metallicity stars. As a consequence, we expect primordial stars to form more massive white dwarf cores than their more metal-rich counterparts, but large uncertainties still remain on the exact form of the mass-loss history.

The first generation of stars has important cosmological consequences. In particular, recent works have shown that adopting zero-metallicity models, instead of the cooler very metal-poor ones, can significantly modify the reionization epoch (e.g., Cojazzi et al. 2000; Tumlinson & Shull 2000; Bromm, Kudritzki, & Loeb 2001). The formation of primordial stellar remnants may also account for some fraction of the Galactic dark matter (e.g., Chabrier 1999). The detection of carbon (e.g., Songaila & Cowie 1996) and nitrogen (e.g., Lu, Sargent, & Barlow 1998) enrichments, as well as of metal lines, in the intergalactic medium at high redshifts suggests primordial AGB stars as strong candidates for the origin of some of these elements (Abia et al. 2001). In the same vein, observations of chemically peculiar metal-poor stars are difficult to explain in the framework of current mixing mechanisms (e.g., Denissenkov et al. 1998), whence the idea of an evolutionary scenario in which a first generation of stars pollutes the proto–globular cluster cloud, producing initial abundance anomalies that survive and are observed nowadays in Population II stars. These examples illustrate only a few of the relevant issues associated with the unique evolutionary properties of the first stars. A more extended study, covering an even larger parameter space than the present work, as well as a better understanding of some of the physical processes are needed to address all of these issues.

The authors gratefully acknowledge valuable comments by an anonymous referee. These comments have significantly improved the presentation of this paper. L. S. wishes to thank the STScI and Monash Department of Mathematics and Statistics for their hospitality during his successive visits. This work has been funded in part by the grant 938-COS191 from the John Templeton Foundation, the Australian Research Council, and the French-Australian International Program for Scientific Collaboration " Stellar Populations, Dark Matter, and Galaxy Surveys." L. S. also acknowledges support from a European TMR " Marie Curie " fellowship at ULB.

REFERENCES

Abia, C., et al. 2001, ApJ, 557, 126
Alexander, D. R., & Ferguson, J. W. 1994, ApJ, 437, 879
Angulo, C., et al. 1999, Nucl. Phys. A, 656, 3
Bonifacio, P., & Molaro, P. 1997, MNRAS, 285, 847
Bromm, V., Coppi, P. S., & Larson, R. B. 1999, ApJ, 527, L5
Bromm, V., Kudritzki, R. P., & Loeb, A. 2001, ApJ, 552, 464
Burles, S., & Tytler, D. 1998, ApJ, 499, 699
Busso, M., Gallino, R., Lambert, D. L., Travaglio, C., & Smith, V. V. 2001, ApJ, 557, 802
Busso, M., Gallino, R., & Wasserburg, G. J. 1999, ARA&A, 37, 239
Cameron, A. G. W., & Fowler, W. A. 1971, ApJ, 164, 111
Carlberg, R. G. 1981, MNRAS, 197, 1021
Cassisi, S., & Castellani, V. 1993, ApJS, 88, 509
Castellani, V. 2000, in Proc. MPA/ESO Astrophysics Workshop, The First Stars, ed. A. Weiss, T. G. Abel, & V. Hill (Garching: ESO), 85
Castellani, V., Gianone, P., & Renzini, A. 1971a, Ap&SS, 10, 340
———. 1971b, Ap&SS, 10, 355
Caughlan, G. R., & Fowler, W. A. 1988, At. Data Nucl. Data Tables, 40, 283
Chabrier, G. 1999, ApJ, 513, L103
Chieffi, A., Dominguez, I., Limongi, M., & Straniero, O. 2001, ApJ, 554, 1159 (C01)
Chieffi, A., & Tornambé, A. 1984, ApJ, 287, 745
Chiosi, C. 2000, in Proc. MPA/ESO Astrophysics Workshop, The First Stars, ed. A. Weiss, T. G. Abel, & V. Hill (Garching: ESO), 95
Cojazzi, P., Bressan, A., Lucchin, F., Pantano, O., & Chavez, M. 2000, MNRAS, 315, L51
Cox, J. P., & Guili, R. T. 1968, in Principles of Stellar Evolution, Vol. 1 (New York: Gordon and Breach), 281
D'Antona, F. 1982, A&A, 115, L1
de Jager, C., Nieuwenhuijzen, H., & van der Hucht, K. A. 1988, A&AS, 72, 259
Denissenkov, P. A., Da Costa, G. S., Norris, J. E., & Weiss, A. 1998, A&A, 333, 926
Despain, K. H. 1981, ApJ, 251, 639
Dominguez, I., Straniero, O., Limongi, M., & Chieffi, A. 2000, in The Changes in Abundances in Asymptotic Giant Branch Stars, ed. F. D'Antona & R. Gallino, in press
Forestini, M., & Charbonnel, C. 1997, A&AS, 123, 241
Frost, C., Cannon, R. C., Lattanzio, J. C., Wood, P. R., & Forestini, M. 1998a, A&A, 332, L17
Frost, C., & Lattanzio, J. C. 1996, ApJ, 473, 383
Frost, C., Lattanzio, J. C., & Wood, P. R. 1998b, ApJ, 500, 355
Fujimoto, M. Y. 1977, PASJ, 29, 331
Fujimoto, M. Y., Iben, I., Chieffi, A., & Tornambé, A. 1984, ApJ, 287, 749
Fujimoto, M. Y., Iben, I., & Hollowell, D. 1990, ApJ, 349, 580 (FIH90)
Fujimoto, M. Y., Ikeda, Y., & Iben, I. 2000, ApJ, 529, L25
Gnedin, N. Y. 2000, ApJ, 535, 530
Goriely, S., & Siess, L. 2001, A&A, 378, L25
Graboske, H. C., DeWitt, H. E., Grossman, A. S., & Cooper, M. S. 1973, ApJ, 181, 457
Herwig, F., Blocker, T., & Driebe, T. 1999, in The Changes in Abundances in Asymptotic Giant Branch Stars, ed. F. D'Antona & R. Gallino, in press
Herwig, F., Blocker, T., Schonberner, D., & El Eid, M. 1997, A&A, 324, L81
Hollowell, D., Iben, I., & Fujimoto, M. Y. 1990, ApJ, 351, 245
Hubbard, W. B., & Lampe, M. 1969, ApJS, 18, 297
Iben, I. 1975, ApJ, 196, 525
———. 1976, ApJ, 208, 165
Iben, I., & Renzini, A. 1982, ApJ, 263, L23
Iglesias, C. A., & Rogers, F. J. 1996, ApJ, 464, 943
Itoh, N., Kohyama, Y., Matsumoto, N., & Seki, M. 1984, ApJ, 285, 758
Itoh, N., Mitake, S., Iyetomi, H., & Ichimaru, S. 1983, ApJ, 273, 774
Langer, N., Heger, A., Wellstein, S., & Herwig, F. 1999, A&A, 346, L37
Lattanzio, J., Pettini, M., Tout, C. A., & Carigi, L. 2001, A&A, submitted
Lu, L., Sargent, W. L. W., & Barlow, T. A. 1998, AJ, 115, 55
Marigo, P., Girardi, L., Chiosi, C., & Wood, P. R. 2001, A&A, 371, 152
Mengel, J. G., & Sweigart, A. V. 1981, in Astrophysical Parameters for Globular Clusters, ed. A. G. D. Philip (Dordrecht: Reidel), 277
Mitake, S., Ichimaru, S., & Itoh, N. 1984, ApJ, 277, 375
Nakamura, F., & Umemura, M. 1999, ApJ, 515, 239
———. 2001, ApJ, 548, 19
Palla, F., Salpeter, E. E., & Stahler, S. W. 1983, ApJ, 271, 632
Pols, O. R., Tout, C. A., Eggleton, P. P., & Han, Z. 1995, MNRAS, 274, 964
Raikh, M. E., & Yakovlev, D. G. 1982, Ap&SS, 87, 193
Schaller, G., Schaerer, D., Meynet, G., & Meader, A. 1992, A&AS, 96, 269
Schlattl, H., Cassisi, S., Salaris, M., & Weiss, A. 2001, ApJ, 559, 1082
Siess, L., Dufour, E., & Forestini, M. 2000, A&A, 358, 593
Silk, J. 1977, ApJ, 211, 638
Songaila, A., & Cowie, L. L. 1996, AJ, 112, 335
Straniero, O., et al. 1997, ApJ, 478, 332
Travaglio, C., et al. 2001, ApJ, 559, 909
Tumlinson, J., & Shull, J. M. 2000, ApJ, 528, L65
Weiss, A., Cassisi, S., Schlattl, H., & Salaris, M. 2000, ApJ, 533, 413 (W00)
Yoshii, Y., & Saio, H. 1986, ApJ, 301, 587